# Multimodal Soft Robotic Actuator Modeling and Validation

Sanjaya Mallikarachchi<sup>1</sup>, P. D. S. Hiroshan Gunawardane<sup>2</sup>, Xuan Tung Le<sup>3</sup>, M. Chiao<sup>2</sup>, Isuru S. Godage<sup>4</sup>

Abstract—The multimodal Zig-zag Soft Pneumatic Actuator (SPA) provides an effective design approach for achieving desired extensions and bending geometries under specific pressure conditions. The rigid-body approximated model introduced in this study brings valuable insights into SPA dynamics by enabling faster simulations when compared to methods such as Finite Element Analysis (FEA). The model outlined in this paper forecasts static behavior by estimating the linear expansion of linear SPA and the bending angle of bending SPA. These two modes of motion can be combined to expand the degree of freedom. Depending on the configuration of the Strain Limiting Layer (SLL), the bending angle can be adjusted by controlling the actuator stiffness, a parameter that can be precisely characterized using the proposed actuator model. To address the hysteresis phenomena in linear expansion SPA, the Bouc-Wen hysteresis model is employed to model the actuator hysteresis responses at higher actuation rates. The validity of the proposed model is experimentally confirmed through the use of 3D-printed SPA prototypes that are designed for both extension and bending actuation.

## I. INTRODUCTION

Soft robotics has garnered considerable attention as a compelling substitute for rigid-body robotic systems, which face numerous constraints and limitations. These challenges include reduced flexibility attributed to rigidity, the necessity for redundant degrees of freedom in rigid robots, and complexities in human-robot interactions [1]. Soft robots, constructed from compliant materials, exhibit notable advantages in terms of flexibility and suitability for a wide array of complex robotics applications [2]-[5]. 3D-printing technology has been explored as a method for the fabrication of soft pneumatic actuators (SPAs) [3]. Nevertheless, developing high-performance SPAs through cost-effective 3D printing techniques, such as fused deposition modeling, presents a formidable challenge [3], [4]. The Zig-zag SPA design is one of the key approaches that was recently investigated to develop multi-modal high-performance SPAs that can be easily adaptable for omni-purpose applications [6].

The proposed SPA design draws inspiration from membrane-type SPAs, such as the PneuNet design, commonly manufactured through molding and casting methods

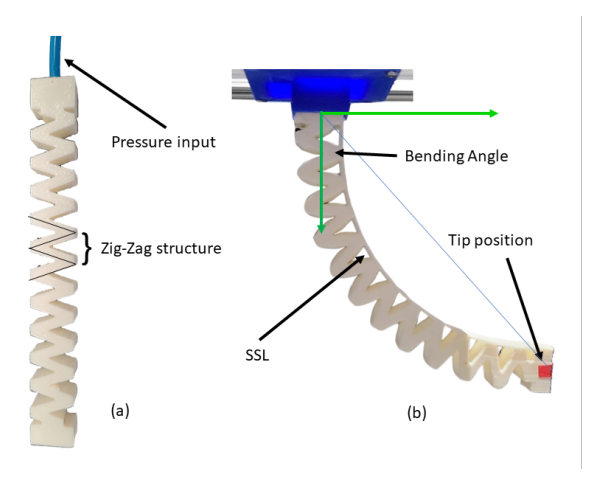


Fig. 1: 3D-printed multimodal Zig-zag SPAs. (a) Linear expansion SPA with no SLL. (b) Bending SPA with one-sided SLL.

[7]-[10]. The novel SPA design primarily entails a springlike structure [6], [11] engineered to achieve a heightened extension relative to its minimal attained thickness as an actuator. Each individual chamber within the SPA maintains a uniform cross-section and is internally interconnected with consecutive chambers at an angle of 45°. Upon the application of pressure, the individual SPA chambers undergo expansion, with the expansion process centering around the connections between each consecutive chamber, ultimately resulting in a cumulative extension at the SPA's tip. Notably, the SPA exhibits a characteristic curve marked by a linear behavior, thereby establishing a proportional relationship between applied pressure, the stiffness constant, and the extension of the SPA. In order to achieve bending motion in the linear SPA, a continuous and uniform thin constraint has been introduced into the 3D printing design. This constraint utilizes the same actuator material (TPU) and is applied to one of the two sides of the SPA. Consequently, it restricts the linear movement of the SPA, generating an imbalance in forces that causes the SPA to flex toward the side where the constraint (strain limiting layer SLL) has been introduced (see Fig. 1).

Modeling these multimodal SPAs for distinct structural configurations presented in this paper by utilizing a generalized model is still a challenging task. In general, to model soft robots, various models have been proposed. One such model category is continuum mechanics models. Under these techniques, Cosserat Rod Theory (CRT), Kirchhoff, and nonlinear Euler Bernoulli beam theories have been employed to model soft robotic actuators [12]. CRT can accurately represent the localized twisting effect [13]–[15]. However, CRT is

<sup>&</sup>lt;sup>1</sup>Department of Multidisciplinary Engineering, Texas A&M University, College Station, TX 77843, USA.

Corresponding author: sanjayadpf@tamu.edu

<sup>&</sup>lt;sup>2</sup>Department of Mechanical Engineering, The University of British Columbia Vancouver, Canada.,

<sup>&</sup>lt;sup>3</sup>J. Mike Walker '66 Department of Mechanical Engineering, Texas A&M University, College Station, TX 77843, USA.,

<sup>&</sup>lt;sup>4</sup>Department of Engineering Technology & Industrial Distribution, J. Mike Walker '66 Department of Mechanical Engineering (affiliated), and Department of Multidisciplinary Engineering (affiliated), Texas A&M University, College Station, TX 77843, USA.

usually computationally intensive and not easily adaptable to varying structural configurations that are utilized in the Zigzag SPA design presented in this paper. Kirchoff and Euler Bernoulli beam theories are less computationally expensive compared to CRT but again fail to model complex SPA shapes and utilize varying structural configuration changes described in the bending SPA in this paper even with the available toolboxes [16] or first principle derivations [13]. Geometrical models such as piecewise constant curvature (PCC) commonly have been employed to model soft actuators [17]. These models use generalized coordinates to represent the geometry of the SPA. PCC models simplify the SPA geometry into curvatures and are more desirable for real-time control with the kinematics models [18], [19] and subsequently deriving the dynamic model using lagrangian mechanics [20]-[23]. Nevertheless, these models lack an accurate representation of SPA dynamics. Numerical techniques are another commonly used technique to model SPAs. Finite element analysis (FEA) is one such commonly used numerical modeling technique for modeling soft actuators [24]–[27]. While this method can model the SPA very accurately, FEA requires a lot of computational power which is not suitable for actuators with very complicated structures and varying structural configurations. This drawback also means that it is very hard to use the model for designing a controller of the actuator. Efficient FEA simulations have been introduced using Simulation Open Framework Architecture (SOFA) [28]. However, it is still complicated to customize for specific soft robotic structures and integrate with other systems hence making the simulation framework less adapted by the robotics community. But it is now slowly gaining popularity within the soft robotic community and recently released newer features in their multi-material FEM plugin [29] for efficient FEA simulations.

Considering the level of model complexity, accuracy of the model, and adaptability for varying structural configurations, discretized modeling techniques are far more effective approximations that can easily employed even for real-time controlling. Soft robot modeling techniques such as pseudo rigid body (PRB) [30] modeling, lumped mass models [31] and discrete rods [32] fall under discretized modeling techniques. Lumped mass models represent the continuous structure by discrete masses, dampers, and springs while PRB uses rigid links that are connected by revolute, universal, or spherical joints [30]. The discrete rod method represents the soft structure as discrete elastic rods (DER) [32] similar to the CRT but in a discretized fashion. For multimodal SPA described in this paper PRB model can be easily adapted to model the varying structural behavior due to SLL.

This paper presents a discretized rigid body approximation model similar to PRB for Zig-zag SPAs by leveraging the Matlab Simscape multibody dynamics toolbox. Section II delves into the dynamic model of the SPA, while Section III elaborates on the SPA's design and the experimental setup employed. Section IV encompasses the presentation of experimental results and model validation, and Section V offers a comprehensive discussion of the conclusions drawn

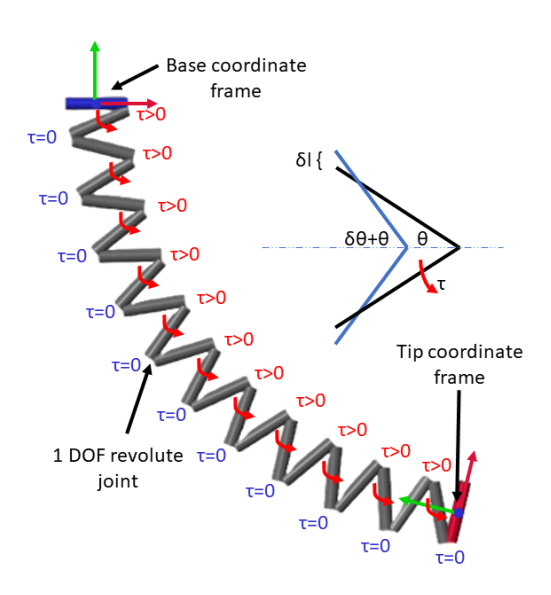


Fig. 2: Rigid body approximated model in Matlab Simscape. The  $\tau$  values that are represented in color blue show the effect of SLL and  $\tau$  values that are represented in red color show the effect due to applied pressure. By applying the  $\tau$  value in opposite directions linear expansion can be obtained from the same model. The geometry of one revolute joint when torque is exerted is shown beside.

from this study.

#### II. DYNAMIC MODEL OF ZIG-ZAG SPA

In order to investigate the dynamic characteristics of the Zig-zag SPA, we introduce a discretized rigid-body approximated dynamic model, as illustrated in Fig. 2. This modeling approach serves to streamline the system's dynamics, transforming it into a rigid-body approximation with cylindrical elements, thereby enabling efficient computations for multibody dynamics analysis. The rigid-body model comprises a sequence of revolute joints that are activated in succession to achieve both linear expansion and bending behaviors. The equation governing the motion of the entire system can be represented by the following (1), employing standard notation where M represents the inertia matrix, C represents the Coriolis and centripetal forces matrix, and G represents the gravity vector. The input torque matrix denoted as  $\tau_{input}$  matrix.

$$M(q)\ddot{q} + C(q, \dot{q})\dot{q} + G(q) = \tau_{input}$$
 (1)

## A. Simscape Model

We employed the MATLAB SimScape Multibody Dynamics toolbox to implement the rigid-body approximate dynamic model, which utilizes efficient multibody dynamics techniques to derive the ordinary differential equations. This approach offers significantly enhanced computational efficiency, particularly suited for tree-structured systems, a category encompassing the majority of robotic manipulators. Notably, the extension and bending behaviors are individually modeled by introducing distinct torque sequences.

1) Linear Zig-zag SPA Model: The linear expansion motion of the Zig-zag SPA is achieved through the application of torques in opposing directions to adjacent revolute joints within the rigid-body approximated model. The input torque matrix, as defined in (1), is structured according to the following torque sequence matrix to obtain the linear expansion.

$$\boldsymbol{\tau_{input}} = \begin{bmatrix} \tau_1 & -\tau_2 & \tau_3 & -\tau_4 & \dots & \tau_n \end{bmatrix}^T$$
 (2)

2) Bending SPA Model: In the case of bending behavior, torques are exclusively applied to odd-indexed joints, whereas joints with even indices receive zero torque. This arrangement is designed to produce the bending response induced by the SLL. The utilization of this torque sequence is motivated by the constraints imposed by the SSL, that effectively restricts rotational motion at the revolute joint. Hence, joints that are immobilized by the SLL receive zero torque. The input torque matrix shown in (1) adheres to the torque sequence matrix delineated below for achieving bending behavior.

$$\boldsymbol{\tau_{input}} = \begin{bmatrix} \tau_1 & 0 & \tau_3 & 0 & \dots & \tau_n \end{bmatrix}^T$$
 (3)

## B. Stiffness Model

In order to model the rotational stiffness of the SPA we experiment to measure its linear stiffness  $(k_l)$  by hanging a known weight. Thereby the total elongation is measured due to the known weight. Then the elongation due to the rotation of each segment  $\delta l$  is calculated for each rigid segment. Where the total number of rigid segments is n. The total force F due to the known weight can be derived using Hook's law. To characterize the stiffness of the SPA, an experimental procedure is undertaken to measure its linear stiffness  $(k_l)$ . This involves suspending a known weight of 50 g and measuring the resulting total elongation. Subsequently, the elongation attributed to the rotation of each rigid segment  $\delta l$  is computed for each segment within the structure. The total count of rigid segments is denoted as n. By employing Hooke's Law, the total force F generated by the known weight is determined. The torque acting on each segment due to the applied weight can be derived, with d representing the length of an individual rigid cylindrical element within the rigid-body model. Additionally, with regard to rotational stiffness  $k_{\theta}$ , the torque can be derived. In accordance with the geometrical configuration depicted in Fig. 2, the elongation  $\delta l$  due to the rotation of each segment can be expressed as specified in (4), where  $\theta$  represents the initial angle of the actuator.

$$\delta l = d\sin(\theta + \delta\theta) - d\sin\theta \tag{4}$$

By employing (4) and substituting the relevant terms, we can determine the rotational stiffness  $k_{\theta}$  as follows.

$$k_{\theta} = \frac{Fd}{2\left[\sin^{-1}\left(\frac{F}{dnk_{l}} + \sin\theta\right) - \theta\right]}$$
 (5)

**TABLE I:** The design parameters and comprehensive specifications of the fabricated linear and bending multimodal Zig-zag SPA.

| Parameter                            | Value               |
|--------------------------------------|---------------------|
| Length(L)                            | $134\mathrm{mm}$    |
| Width(W)                             | $16\mathrm{mm}$     |
| Height(H)                            | $13\mathrm{mm}$     |
| Wall thickness [chambers] (t)        | $0.6\mathrm{mm}$    |
| Chamber angle $(\alpha)$             | 45°                 |
| Pressure range $(\delta P)$          | $0-350\mathrm{kPa}$ |
| Extension range $(\delta L)$         | $0-40\mathrm{mm}$   |
| Strain-limiting-layer thickness (s)  | $0.5\mathrm{mm}$    |
| Mass(m)                              | 13 g                |
| Bending angle range $(\delta\theta)$ | 0-100°              |

For each pressure applied to the linear SPA, the complete linear displacement is measured, and the rotational stiffness is determined using (5). Subsequently, the torque applied to the rigid-body approximated model is optimized through the utilization of MATLAB's *fmincon* function. The objective function employed for optimization seeks to minimize the error in y-axis' displacement of the linear expansion SPA.

Upon establishing the pressure-torque relationship through the linear expansion SPA, this same relationship is subsequently applied to actuate the model of the bending SPA. The bending SPA was fabricated with different configurations designed to elicit distinct tip movements, as explained in the design Section (see Fig. 5). For each of these configurations, stiffness is optimized once more, utilizing the MATLAB *fmincon* function. The optimization objective is centered on minimizing the error in bending angles. It is assumed that the torque exerted on the rigid-body approximate model remains consistent across all revolute joints.

## C. Hysteresis Model

The hysteresis within the linear SPA and bending SPA is represented by the Bouc-Wen hysteresis model, which is particularly well-suited for capturing hysteresis phenomena in a spring-mass-damping system. For a given force F(t), displacement u(t), and velocity  $\dot{u}(t)$ , the Bouc-Wen model defines hysteresis using a component denoted as hysteretic displacement z(t), as expressed in (6).

$$\dot{z}(t) = A\dot{u}(t) - \beta \dot{u}(t)|z(t)|z(t)^{n-1} - \alpha \dot{u}(t)z(t)^{n}$$
 (6)

where A,  $\alpha$ ,  $\beta$  and n are Bouc-Wen parameters.

The force and displacement relationship in a hysteretic system is expressed as

$$F(t) = ku(t) + c\dot{u}(t) + kz(t) \tag{7}$$

where k and c represent the stiffness and damping coefficients respectively.

#### III. FABRICATION AND EXPERIMENTAL SETUP

## A. SPA Fabrication Process

The CAD files of the multimodal Zig-zag SPA were prepared using SolidWorks 2023, subsequently sliced utilizing Simplify3D, and then 3D-printed using Flash Print

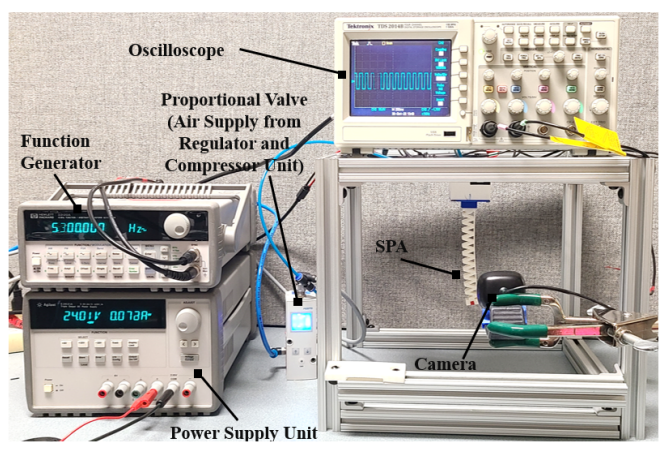


**Fig. 3:** Experimental setup employed for SPA characterization, featuring the utilization of a function generator for the input of diverse pressure signals to the SPAs.

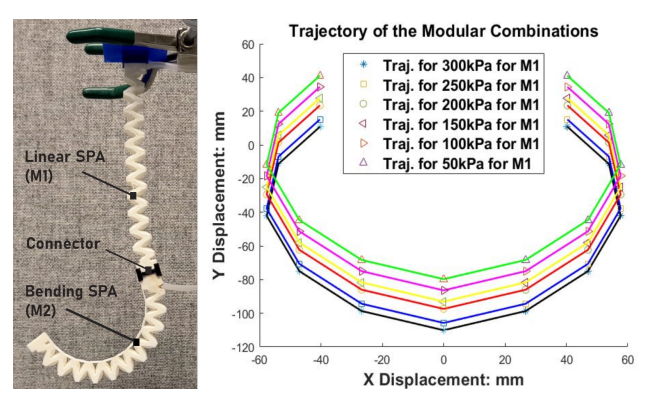


**Fig. 4:** Integration of linear and bending SPAs for complex tip movements. This illustration showcases the simultaneous operation of a single linear SPA and a bending SPA, resulting in combined and coordinated tip movements.

5 software. The chosen 3D printer for this purpose was the Flash Forge Dreamer NX, equipped with a dual extruder system. The printing material employed was Ninja Flex Snow, with a diameter of 1.75 mm and a hardness rating of 95A -Thermoplastic Polyurethane (TPU). The specific printer settings, mentioned in [6], [33], [34], were used throughout the fabrication process. To optimize the printing procedure, the SPA fabrication was conducted without the upper cover of the 3D printer, thereby enhancing air circulation within the 3D printer. The total duration for the 3D printing of the SPA amounted to approximately 9.5 hours in total, representing a significant advancement in efficiency when compared to the traditional molding and casting technique (comprehensive production process, encompassing 3D printing of molds, the fabrication of parts, and their subsequent assembly, is characterized by a longer duration when compared to the time required solely for 3D printing in the context of membranetype SPAs). Both the linear SPA and the bending SPA designs underwent 3D printing under identical printer conditions. Subsequently, air tubes were inserted into the structural components through precise press-insertion, facilitated by small apertures accommodating the pressure input.



**Fig. 5:** Distinct SLL configurations of the bending SPA. T1 represents the continuous SLL, while T2 and T6 correspond to discontinuous SLLs that result in varying bending angles.

## B. SPA Experiment Setup

The experimental configuration for the SPA was primarily devised with a specific focus on characterizing the SPA. The experimental setup (see Fig. 3) comprises a base that allows both types of SPAs to be suspended vertically, while their actuation is visually monitored through the use of web cameras. For lower-speed movements, a Microsoft Life Cam HD 3000 camera was employed, whereas for highspeed movements, a Samsung S20 Plus mobile phone camera capable of recording at 4K resolution and 60 frames per second was utilized. The recorded SPA movements were subsequently subjected to analysis, facilitated by Tracker version 6.1.3, which involved the calibration of individual frames extracted from the video footage. To execute the experimental setup, pressurized air was generated by a SPEEDAIRE compressor, regulated by the AURORA 1.4 MPa air regulator. The precise control of pressure during experimentation was achieved through a FESTO proportional pressure regulator (model VPPM-6L-L-1G18-0L10H-V1P-S1C1). The operation of this regulator was controlled using a power supply (GWINSTEK GPS-3303) and a function generator (HEWLET PACKARD 33120A), which were connected to the valve. All collected data underwent an initial processing phase through the Tracker software, followed by more comprehensive preprocessing and analysis in the MATLAB R2023b software environment.

To evaluate the modular configurations of distinct bending and linear SPAs, a serial connection was established among the SPAs utilizing 3D-printed press-fittable PLA connectors, as illustrated in Fig. 4. To generate a variation of trajectories from the bending SPAs, SLL were fabricated via 3D printing, featuring varying thicknesses (see Table II) and configurations (see Fig. 5). The extent of bending was quantitatively assessed by measuring the bending angle formed by the line connecting the actuator's base to its tip, relative to its initial resting position for different pressure inputs.

#### IV. RESULTS

The primary objective of the experimentation was to characterize the SPAs. Initially, controlled step inputs were applied to both the linear and bending SPA variations. Subsequently, the observed alterations in actuator extension and bending angle were recorded and utilized in the derivation of model parameters. These parameters were further leveraged to establish the relationship between model torque and the

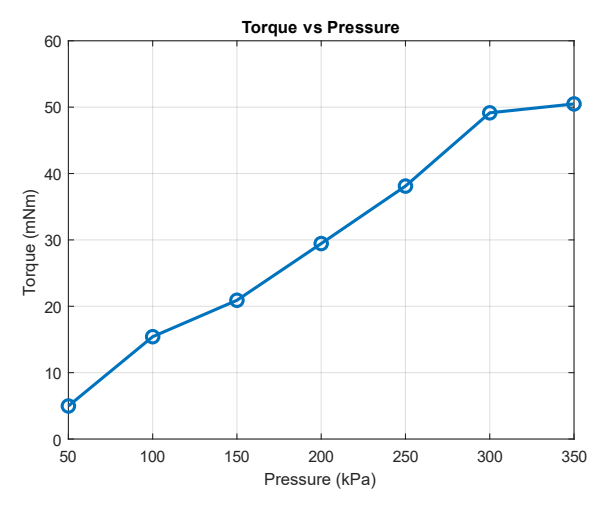


**Fig. 6:** Torque vs. Pressure relationship for experimentally derived rotational stiffness  $k_{\theta} = 1.3296 \text{ N m rad}^{-1}$  for the linear expansion SPA.

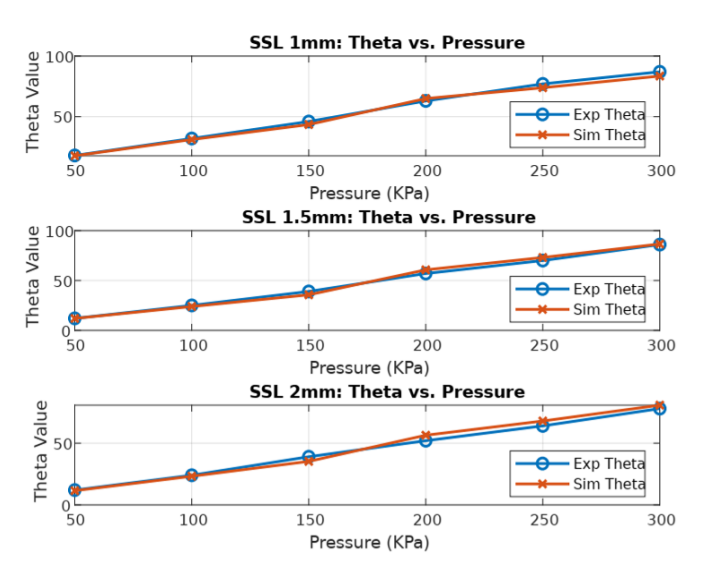


Fig. 7: Simulated and experimental bending angles for distinct SSL thicknesses.

experimental setup pressure, predicated on the observed extensions and bending angles. Furthermore, the stiffness of the bending actuator was determined using the same torque vs. pressure relationship.

## A. Torque and Pressure Relationship

Initially, a mass of  $50\,\mathrm{g}$  was suspended. Subsequently, linear stiffness values were determined for each applied pressure condition. The analysis revealed that the linear stiffness values exhibited minimal variation. Therefore, an average linear stiffness  $k_l$  was computed, which was subsequently employed in the calculation of the rotational stiffness  $k_\theta$  for the simplified rigid body model in SimScape, yielding a value of  $1.3296\,\mathrm{N}\,\mathrm{m}\,\mathrm{rad}^{-1}$ . The graphical representation in Fig. 6 illustrates the converged torque values corresponding to the increasing pressure inputs.

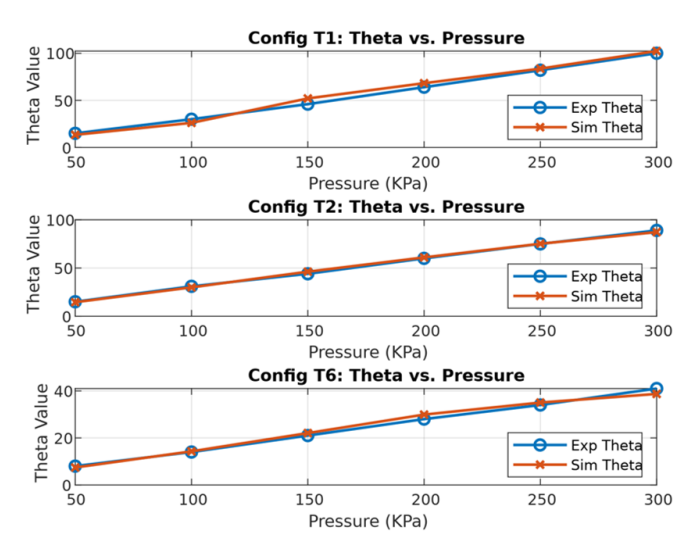


Fig. 8: Simulated and experimental bending angles for distinct SSL configurations

**TABLE II:** SSL thicknesses and optimized  $k_{\theta}$ .

| SSL Thickness (mm) | <b>Optimized</b> $k_{\theta}$ (N m rad <sup>-1</sup> ) |
|--------------------|--|
| 1                  | 0.14791  |
| 1.5                | 0.1538   |
| 2                  | 0.1659   |

## B. Bending Actuator Stiffness

Subsequently, the torque vs. pressure relationship obtained was employed for the optimization of stiffness across three distinct SSL thicknesses. The objective of this optimization was to attain the experimentally observed bending angles for each pressure input. Notably, the variations in stiffness were primarily governed by the characteristics of the SSL, resulting in the influence of pressure changes on stiffness being negligible. Each SPA with increasing SSL thickness showed a mean absolute error of  $2.03^{\circ}$ ,  $1.97^{\circ}$ , and  $2.69^{\circ}$ . While the standard deviations are  $1.27^{\circ}$ ,  $1.57^{\circ}$ , and  $1.68^{\circ}$  respectively. The respective stiffness values are shown in Table II and the bending angle variation for each SSL thickness is shown in Fig. 7.

#### C. Combined Actuation

The combination of the linear expansion SPA and the bending SPA can be integrated to achieve a higher degree of freedom, tailored to the specific requirements of the application. Utilizing the consistent pressure and torque relationship, both the model and the physical prototype are actuated, enabling the resulting task space depicted in Fig. 4. The absolute mean error between simulated SPAs and the prototype are respectively  $2.2\,\mathrm{mm}$  for linear expansion SPA and  $3.1^\circ$  for bending SPA for the combined arrangement.

## D. Bending for Varying SLL Parameters

Experiments were conducted to study the variations in bending angles achievable through the modification of the bending actuator structure, involving the introduction of discrete layers of SLL. In the T1 configuration, a uniform SSL layer with a thickness of 0.6 mm was employed, while

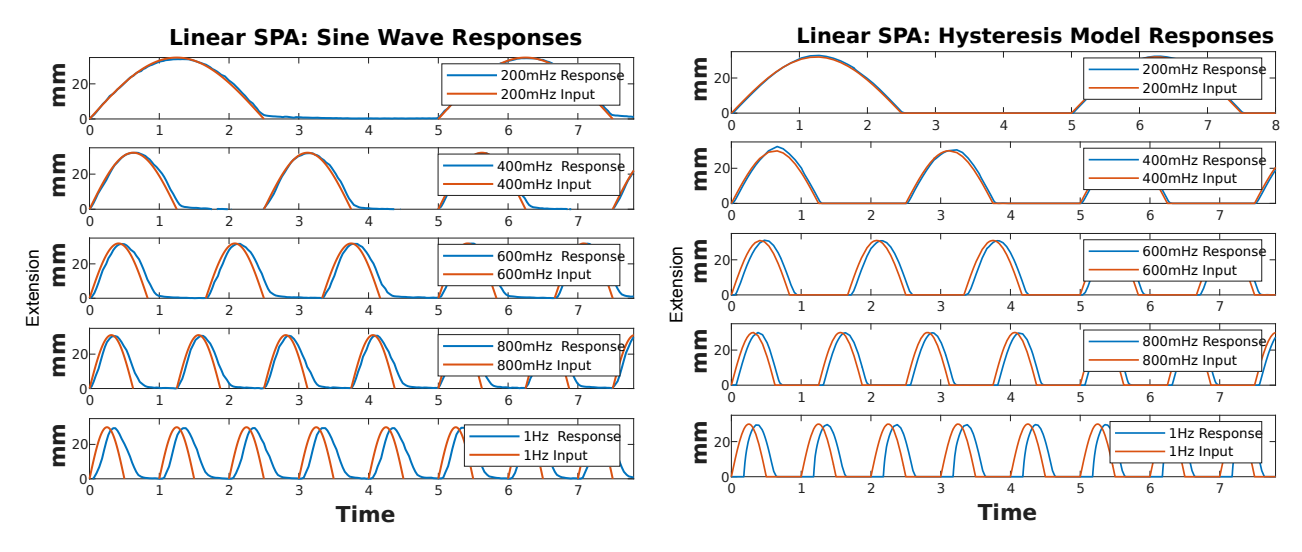


Fig. 9: Linear expansion SPA response for Sinusodal inputs 0.2-1 Hz and dynamic model response with Bouc-Won hysteresis model.

the T2 and T6 actuators featured discretized SSL layers with a similar thickness, as illustrated in Fig. 5. Applying the identical torque vs. pressure relationship as depicted in Fig. 6 to these SLL configurations, a diverse range of bending angles was successfully achieved, resulting in an enhanced rotational stiffness  $(k_{\theta})$ . This afforded us the capability to manipulate  $k_{\theta}$  to achieve the desired bending angles. The experimental bending angles of the prototype, alongside the simulated bending angles, are shown in Fig. 8. Each SPA with distinct SSL configurations showed a mean absolute error of  $3.29 \pm 1.75^{\circ}$ ,  $1.10 \pm 0.76^{\circ}$ , and  $1.19 \pm 0.77^{\circ}$ .

## E. Hysterysis Analysis

In addition to conventional step input tests, a series of frequency tests were undertaken over a frequency range from 0 to 1 Hz. These tests encompassed the application of continuous sine waveforms, each emulating step, sinusoidal, and ramp inputs, sustained for approximately 30 s. These waveforms were administered to the SPAs with an amplitude of 336 kPa and a zero offset (0 mV), spanning a diverse array of frequencies within the specified frequency range. The responses of the SPAs to this spectrum of frequencies were recorded, and it was observed that the extending Zig-zag SPA exhibited hysteresis in frequencies exceeding 0.6 Hz and the Hysterisis displacement is modeled up to 1 Hz iteratively tuning the Bouc Wen model parameters. Responses are depicted in Fig. 9.

To characterize the hysteresis response of the actuator, we employ the Bouc–Wen hysteresis model, as detailed in Section II. In the context of the Bouc–Wen hysteresis model, it is required to determine the damping coefficient of the system. This necessitates subjecting the Zig-zag SPA to a step input. The resulting response exhibits a behavior akin to that of an overdamped response (see Fig. 10).

## V. CONCLUSION

This paper introduces a rigorous, simplified model for the analysis of 3D-printed multimodal Zig-zag-shaped SPAs.

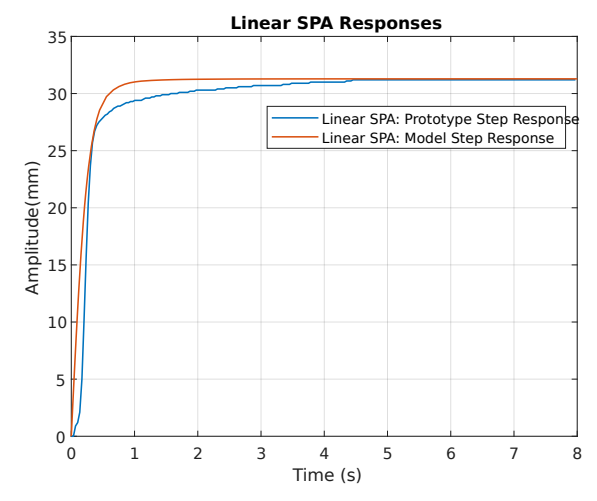


Fig. 10: Step response of linear Zig-zag SPA and step response of the Simscape model.

These SPAs utilize pneumatic pressure for both extension and bending operations. Leveraging this rigid-body model expedites the simulation of the dynamics of these soft actuators and enhances their usability. The linear extension model, as detailed in this study, forecasts the static behavior of the linear SPA by optimizing torque and establishing the relationship between torque vs. pressure inputs. Likewise, a bending model is developed to predict the behavior of the bending SPA by optimizing stiffness to achieve desired bending angles. To mitigate hysteresis phenomena, a Bouc-Wen hysteresis model is incorporated to represent the actuator's response when operating at high frequencies. The models proposed in this paper are rigorously validated through experimental implementation on 3D-printed SPA prototypes, encompassing both extension and bending functionalities. Future work includes the expansion of the hysteresis model to incorporate the bending SPA that shows hysteresis in higher frequencies compared to linear expansion SPA and employing advanced optimization criteria to tune the Bouc Won parameters. These validated models will subsequently used for the development of a real-time controller for multimodal Zig-zag SPAs and their diverse applications.

#### ACKNOWLEDGMENT

The authors express their sincere gratitude for the funding sources that have generously supported this research; The Friedman Award for Scholars in Health at UBC, and the NSERC CREATE grant (565429-2022), funding was awarded to P.D.S.H. Gunawardane and M. Chiao. In addition, this work is supported in part by the National Science Foundation (NSF) Grants IIS–2008797, CMMI–2048142, and CMMI–2132994.

#### REFERENCES

- H. Wang, M. Totaro, and L. Beccai, "Toward perceptive soft robots: Progress and challenges," *Advanced Science*, vol. 5, no. 9, p. 1800541, 2018.
- [2] N. El-Atab, R. B. Mishra, F. Al-Modaf, L. Joharji, A. A. Alsharif, H. Alamoudi, M. Diaz, N. Qaiser, and M. M. Hussain, "Soft actuators for soft robotic applications: A review," *Advanced Intelligent Systems*, vol. 2, no. 10, p. 2000128, 2020.
- [3] C. Tawk and G. Alici, "A review of 3d-printable soft pneumatic actuators and sensors: research challenges and opportunities," *Advanced Intelligent Systems*, vol. 3, no. 6, p. 2000223, 2021.
- [4] E. Sachyani Keneth, A. Kamyshny, M. Totaro, L. Beccai, and S. Magdassi, "3d printing materials for soft robotics," *Advanced Materials*, vol. 33, no. 19, p. 2003387, 2021.
- [5] Y. Ye, Z. Wan, P. Gunawardane, Q. Hua, S. Wang, J. Zhu, M. Chiao, S. Renneckar, O. J. Rojas, and F. Jiang, "Ultra-stretchable and environmentally resilient hydrogels via sugaring-out strategy for soft robotics sensing," *Advanced Functional Materials*, p. 2315184, 2024.
- [6] P. Gunawardane, P. Cheung, H. Zhao, G. Alici, C. De Silva, and M. Chiao, "A versatile 3d-printable soft pneumatic actuator design for multi-functional applications in soft robotics," in *Soft Robotics* (Accepted and in production), 2024.
- [7] P. D. S. H. Gunawardane, R. E. A. Pallewela, and N. T. Medagedara, "Tele-operable controlling system for hand gesture controlled soft robot actuator," in 2019 2nd IEEE International Conference on Soft Robotics (RoboSoft). IEEE, 2019, pp. 656–662.
- [8] P. Gunawardane, N. Budiardjo, G. Alici, C. De Silva, and M. Chiao, "Thermoelastic strain-limiting layers to actively-control soft actuator trajectories," in 2022 IEEE 5th International Conference on Soft Robotics (RoboSoft). IEEE, 2022, pp. 48–53.
- [9] G. Alici, T. Canty, R. Mutlu, W. Hu, and V. Sencadas, "Modeling and experimental evaluation of bending behavior of soft pneumatic actuators made of discrete actuation chambers," *Soft robotics*, vol. 5, no. 1, pp. 24–35, 2018.
- [10] B. A. W. Keong and R. Y. C. Hua, "A novel fold-based design approach toward printable soft robotics using flexible 3d printing materials," *Advanced Materials Technologies*, vol. 3, no. 2, p. 1700172, 2018
- [11] A. Zolfagharian, M. P. Mahmud, S. Gharaie, M. Bodaghi, A. Z. Kouzani, and A. Kaynak, "3d/4d-printed bending-type soft pneumatic actuators: Fabrication, modelling, and control," *Virtual and Physical Prototyping*, vol. 15, no. 4, pp. 373–402, 2020.
- [12] C. Armanini, F. Boyer, A. T. Mathew, C. Duriez, and F. Renda, "Soft robots modeling: A structured overview," *IEEE Transactions on Robotics*, 2023.
- [13] F. Boyer, V. Lebastard, F. Candelier, and F. Renda, "Dynamics of continuum and soft robots: A strain parameterization based approach," *IEEE Transactions on Robotics*, vol. 37, no. 3, pp. 847–863, 2020.
- [14] H. B. Gilbert and I. S. Godage, "Validation of an extensible rod model for soft continuum manipulators," in 2019 2nd IEEE International Conference on Soft Robotics (RoboSoft). IEEE, 2019, pp. 711–716.
- [15] Q. Xiao, M. Musa, I. S. Godage, H. Su, and Y. Chen, "Kinematics and stiffness modeling of soft robot with a concentric backbone," *Journal* of Mechanisms and Robotics, vol. 15, no. 5, p. 051011, 2023.

- [16] M. Gazzola, L. Dudte, A. McCormick, and L. Mahadevan, "Forward and inverse problems in the mechanics of soft filaments," *Royal Society open science*, vol. 5, no. 6, p. 171628, 2018. [Online]. Available: https://doi.org/10.1098/rsos.171628
- [17] I. S. Godage, G. A. Medrano-Cerda, D. T. Branson, E. Guglielmino, and D. G. Caldwell, "Modal kinematics for multisection continuum arms," *Bioinspiration & biomimetics*, vol. 10, no. 3, p. 035002, 2015.
- [18] D. D. Arachchige, D. M. Perera, S. Mallikarachchi, U. Huzaifa, I. Kanj, and I. S. Godage, "Soft steps: Exploring quadrupedal locomotion with modular soft robots," *IEEE Access*, 2023.
- [19] D. D. Arachchige, D. M. Perera, S. Mallikarachchi, I. Kanj, Y. Chen, and I. S. Godage, "Wheelless soft robotic snake locomotion: Study on sidewinding and helical rolling gaits," in 2023 IEEE International Conference on Soft Robotics (RoboSoft). IEEE, 2023, pp. 1–6.
- [20] D. D. Arachchige, S. Mallikarachchi, I. Kanj, D. M. Perera, Y. Chen, H. B. Gilbert, and I. S. Godage, "Dynamic modeling and validation of soft robotic snake locomotion," in 2023 9th International Conference on Control, Automation and Robotics (ICCAR). IEEE, 2023, pp. 6–12.
- [21] I. S. Godage, D. T. Branson, E. Guglielmino, G. A. Medrano-Cerda, and D. G. Caldwell, "Shape function-based kinematics and dynamics for variable length continuum robotic arms," in 2011 IEEE International Conference on Robotics and Automation. IEEE, 2011, pp. 452–457.
- [22] I. S. Godage, G. A. Medrano-Cerda, D. T. Branson, E. Guglielmino, and D. G. Caldwell, "Dynamics for variable length multisection continuum arms," *The International Journal of Robotics Research*, vol. 35, no. 6, pp. 695–722, 2016.
- [23] I. S. Godage, R. J. Webster, and I. D. Walker, "Center-of-gravity-based approach for modeling dynamics of multisection continuum arms," *IEEE transactions on robotics*, vol. 35, no. 5, pp. 1097–1108, 2019.
- [24] J. Guo, J.-H. Low, X. Liang, J. S. Lee, Y.-R. Wong, and R. C. H. Yeow, "A hybrid soft robotic surgical gripper system for delicate nerve manipulation in digital nerve repair surgery," *IEEE/ASME Transactions on Mechatronics*, vol. 24, no. 4, pp. 1440–1451, 2019.
- [25] C. M. Thalman and H. Lee, "Design and validation of a soft robotic ankle-foot orthosis (sr-afo) exosuit for inversion and eversion ankle support," in 2020 IEEE International Conference on Robotics and Automation (ICRA), 2020, pp. 1735–1741.
- [26] M. S. Xavier, S. M. Harrison, D. Howard, Y. K. Yong, and A. J. Fleming, "Modeling of soft fluidic actuators using fluid-structure interaction simulations with underwater applications," *International Journal of Mechanical Sciences*, vol. 255, p. 108437, 2023. [Online]. Available: https://www.sciencedirect.com/science/article/pii/S0020740323003399
- [27] P. Polygerinos, Z. Wang, J. T. B. Overvelde, K. C. Galloway, R. J. Wood, K. Bertoldi, and C. J. Walsh, "Modeling of soft fiber-reinforced bending actuators," *IEEE Transactions on Robotics*, vol. 31, no. 3, pp. 778–789, 2015.
- [28] F. Faure, C. Duriez, H. Delingette, J. Allard, B. Gilles, S. Marchesseau, H. Talbot, H. Courtecuisse, G. Bousquet, I. Peterlik et al., "Sofa: A multi-model framework for interactive physical simulation," Soft tissue biomechanical modeling for computer assisted surgery, pp. 283–321, 2012.
- [29] French Institute for Research in Computer Science and Automation, Massachusetts General Hospital. SOFA - Simulation Open Framework Architecture. [Online]. Available: https://www.sofa-framework.org/
- [30] M. Khoshnam and R. V. Patel, "A pseudo-rigid-body 3r model for a steerable ablation catheter," in 2013 IEEE International Conference on Robotics and Automation. IEEE, 2013, pp. 4427–4432.
- [31] H. Habibi, C. Yang, I. S. Godage, R. Kang, I. D. Walker, and D. T. Branson III, "A lumped-mass model for large deformation continuum surfaces actuated by continuum robotic arms," *Journal of mechanisms and robotics*, vol. 12, no. 1, p. 011014, 2020.
- [32] M. Bergou, M. Wardetzky, S. Robinson, B. Audoly, and E. Grinspun, "Discrete elastic rods," in *ACM SIGGRAPH 2008 papers*, 2008, pp. 1–12
- [33] C. Tawk, G. M. Spinks, M. in het Panhuis, and G. Alici, "3d printable linear soft vacuum actuators: their modeling, performance quantification and application in soft robotic systems," *IEEE/ASME Transactions on Mechatronics*, vol. 24, no. 5, pp. 2118–2129, 2019.
- [34] C. Tawk, M. in het Panhuis, G. M. Spinks, and G. Alici, "Bioinspired 3d printable soft vacuum actuators for locomotion robots, grippers and artificial muscles," *Soft robotics*, vol. 5, no. 6, pp. 685–694, 2018.